Joint Special Interest Group meeting between euspen and ASPE
Advancing Precision in Additive Manufacturing
Ecole Centrale de Nantes, France, September 2019
www.euspen.eu

Methodology for geometric characterization and dimensioning of additively manufactured channels

T. Dahmen[1], C. G. Klingaa[1], S. Baier[2], D. B. Pedersen[1], J. H. Hattel[1]

[1]*Department of Mechanical Engineering, Technical University of Denmark, Produktionstorvet, Building 425, 2800 Kgs. Lyngby, Denmark*
[2]*Department of Physics, Technical University of Denmark, Fysikvej, Building 307, 2800 Kgs. Lyngby, Denmark*

tdah@mek.dtu.dk

Abstract

Metal additive manufacturing has the potential to enhance the performance of engineering applications by utilizing its inherent design freedom to create complex geometries such as required for conformal cooling. However, additively manufactured channels show significant form deviations when made by laser powder bed fusion. Thereby, not only process-parameters have an influence, but also design-parameters, such as the assigned build direction and the chosen diameter, matter. From a precision manufacturing point of view, there is a need to understand these interdependencies in order to control the deviations. Hence, this work introduces a standardized methodology to quantify and manage the influence of design-parameters on form deviations under a given set of process-parameters. The methodology utilizes two different kinds of test artefacts that are non-destructively analyzed by X-ray computed tomography and light optical microscopy. The results show a proportional influence of build direction and a degressive influence of diameter on cross-sectional area reductions. A resulting prediction model and lookup table serves as a foundation for design engineers to counteract form deviations by pre-processing the CAD-data accordingly. Moreover, this contribution and its artefacts can be utilized as a standard for benchmarking and process-optimization of additively manufactured channels in the future.

Metal additive manufacturing, design for additive, design guidelines, conformal cooling, laser powder bed fusion, 17-4PH

1. Introduction

A variety of industrial applications such as injection molds, hydraulic equipment, and fuel nozzles utilize additively manufactured channels to exchange heat, transport, or accelerate mass [1-3]. Based on the application, the length and the placement, the performance of these channels are determined by their cross-sectional area, their profile, and their internal surface texture [4].

Additively manufactured channels made by laser powder bed fusion (L-PBF) show significant deviations from conventionally machined channels, especially prominent in the overhanging areas with regard to the building direction [5]. These deviations occur due to the sintering of unfused powder particles of previous layers onto the actual processed layer during melting. Thereby, the unintended sintering is amplified by insufficient heat dissipation through the unfused powder bed [6].

Previous contributions have shown pragmatic approaches to mitigate this effect by adapting the initial CAD-design using “teardrop”- or “diamond”-shaped cross-sectional profiles [7]. However, from a design-point of view, it is not clear how to dimension such complex profile geometries precisely, in particular, because the resulting actual profile after manufacturing is also dependent on the channel direction and its nominal diameter.

Therefore, this work suggests a simplified approach by locking the circular profile of the channel in the initial CAD-design. Thereby, a methodology is introduced to quantify the influence of channel direction and diameter on the resulting actual cross-sectional area of the channel. Finally, prediction models and resulting look-up tables can serve as design guidelines to dimension channels based on a given set of process-parameters.

First, the methodology including the experimental set-up, test artefacts, and measuring techniques are introduced. Second, the methodology is applied, and results are presented and discussed. Finally, a look-up table is presented and further work is addressed.

2. Methodology

This work is following the general methodology described in figure 1.

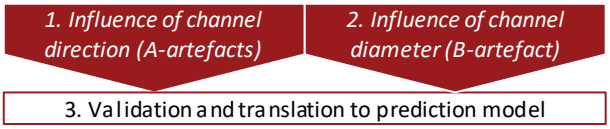

Figure 1. General methodology in this work

2.1. Experimental set-up

Two different types of artefacts were designed and additively manufactured by L-PBF, as shown in figure 2. The first type of artefact is shaped as a cuboid (10 x 10 x 12.5 mm) containing a straight channel with a nominal diameter of two millimeters. There are seven of these cuboids with different channel directions ranging from $\alpha = 0°$ to 90°, where the latter direction is parallel to the build direction. In the following, these cuboids are referred to as A-artefacts. The larger cuboid (15 x 62.5 x 15.5 mm) contains thirteen channels with different diameters ranging from $d_{nominal} = 0.5$ mm to 4.3 mm. Each channel is ‘’L-shaped’’ transitioning in direction from each end

after five straight millimeters from α = 0° to 90° and vice versa. This artefact will be referred to as the B-artefact in the following.

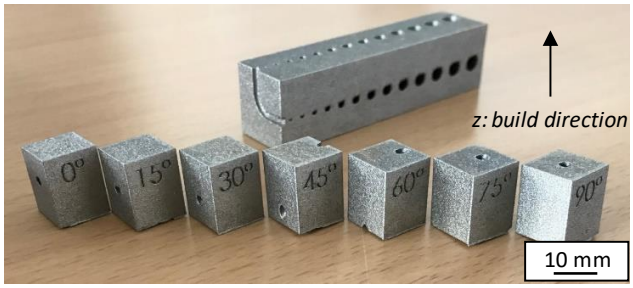

Figure 2. Generated A-artefacts in the front with $d_{nominal}$ = 2 mm and α = 0° to 90° (from left to right), generated B-artefact in the back with $d_{nominal}$ = 0.5 mm to 4.1 mm for α = 0° and 90°

The A- and B-artefacts were generated in the same build job on an EOS M 290 L-PBF system in 17-4PH stainless steel with a layer thickness of Δz_{layer} = 40 µm. More process parameters are shown in table 1. No surface treatments were applied.

Table 1 Used L-PBF process parameters in this work

Process parameters	Value
Laser power, P_L	220.1 W
Scanning speed, v_{scan}	755.5 mm/s
Hatch spacing, Δy_{hatch}	110 µm
Layer height, Δz_{layer}	40 µm
Spot diameter, d_{spot}	100 µm
Build temperature, T_{build}	80°C
Particle size	D50: 36-44 µm

2.2. Image analysis of CT-data for A-artefacts

Computed tomography (CT) and image analysis were used to evaluate the A-artefacts. Each artefact was scanned once with the same parameters using a Nikon XT H 225 ST system with a cone setup, tungsten filament, and a flat panel detector. A voltage of 220 kV, a power of 29.9 W, and a 0.5 mm Sn filter were used. 1571 projections were acquired with an exposure time of one second and two averaged frames per projection. A voxel size of 15.9 µm was obtained with two by two binning. The reconstruction was made using filtered-back projection the X-Tek CT Pro 3D software (Nikon Metrology Inc.).

The software Avizo 9.2. (Thermo Fisher Scientific) was used to export 500 cross-sectional images along the channel direction for each of the seven A-artefacts, as shown in figure 3. Subsequently, an in-house python script was applied to extract and average the cross-sectional area of each image [8].

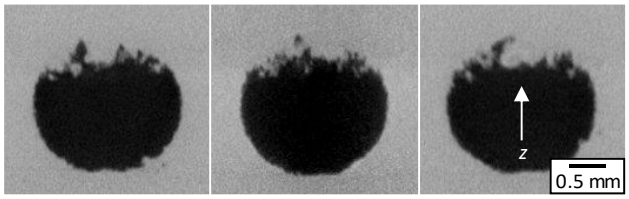

Figure 3. CT-images at different positions along the channel direction for α = 0° and $d_{nominal}$ = 2 mm (beginning, middle and at the end)

2.3. Analysis of LOM images for B-artefact

Light optical microscopy (LOM) and image analysis were used to analyze the B-artefact. Each channel was recorded coaxially from both channel ends by a VHX-6000 digital microscope with a VH-Y20R/Z20T lens (Keyence Corp.).

The image analysis was conducted using the software ImageJ (open source) [9]. The procedure is shown in figure 4. First, unfocused and blurry background was removed (1). Next, the images were converted to grayscale and thresholded (2). Finally, the wand tracing tool was used to extract the cross-sectional profiles and its enclosed areas (3). Each analysis was repeated three times using three different values for the thresholding.

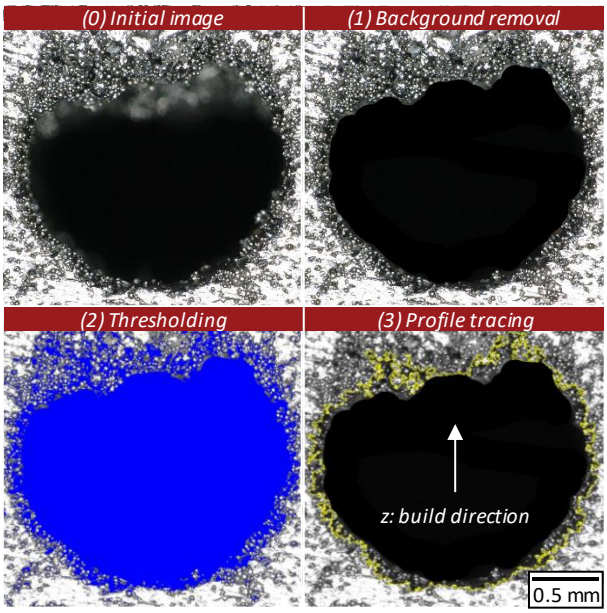

Figure 4. Determination of cross-sectional channel area using LOM and image analysis for $d_{nominal}$ = 2.0 mm and α = 0°

3. Influence of channel direction on actual cross-sectional area

The results from CT-scanning and subsequent image analysis of the A-artefacts are summarized in figure 5. The highest reduction in cross-sectional area is observed for the channel built perpendicular to the build direction (α = 0°). With 3.03 mm² measured actual area, its reduction amounts to -16.1 % when compared to the nominal area of 3.14 mm² of a channel with a nominal diameter of two millimeters. The deviations decrease in an approximately linear manner to -3.4% at α = 90°, where the channel is built parallel to the build direction. Moreover, it is noted that the standard deviation also decreases with an increasing degree of the channel direction from α = 0° to 90°.

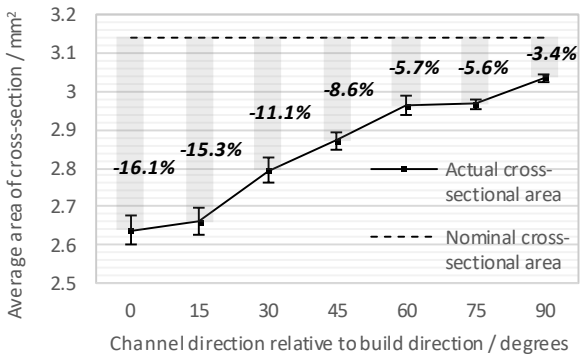

Figure 5. Influence of channel direction α on cross-sectional area for $d_{nominal}$ = 2 mm, based on A-artefacts and image analysis of CT data

In order to quantify the influence of build direction on the actual cross-section for $d_{nominal}$ = 2 mm a simple linear regression model can be used to describe the observed data

(1) $$A_{actual}(\alpha) = 0.071\,\alpha\,\frac{mm^2}{degrees} + 2.564\,mm^2$$

with an R^2-value of 95.83 %.

4. Influence of channel diameter on form deviations

Based on the B-artefact, the image analysis of three cases $d_{nominal}$ = 0.8 mm, 2.3 mm and 3.8 mm for both α = 0° and 90° are shown in figure 6. The channel with $d_{nominal}$ = 0.8 mm and α = 0° shows large agglomerations of powder particles being sintered onto the overhanging area of the channel wall. Consequently, the cross-sectional area is reduced significantly. While the agglomerations of sintered powder particles remain in the overhanging area with an increasing $d_{nominal}$, its relative impact on the actual cross-sectional area is decreasing. Moreover, the cross-sectional profile of the channels is becoming oval-shaped for higher $d_{nominal}$.

For channels with α = 90°, it can be clearly seen that the cross-sectional profile is more circular with an increased area when compared to α = 0°. Yet, a few scattered sintered powder particles are distributed along the channel walls in a random manner. Here again, it can be seen that the relative impact of these particles on the actual cross-sectional area is decreasing with increasing $d_{nominal}$.

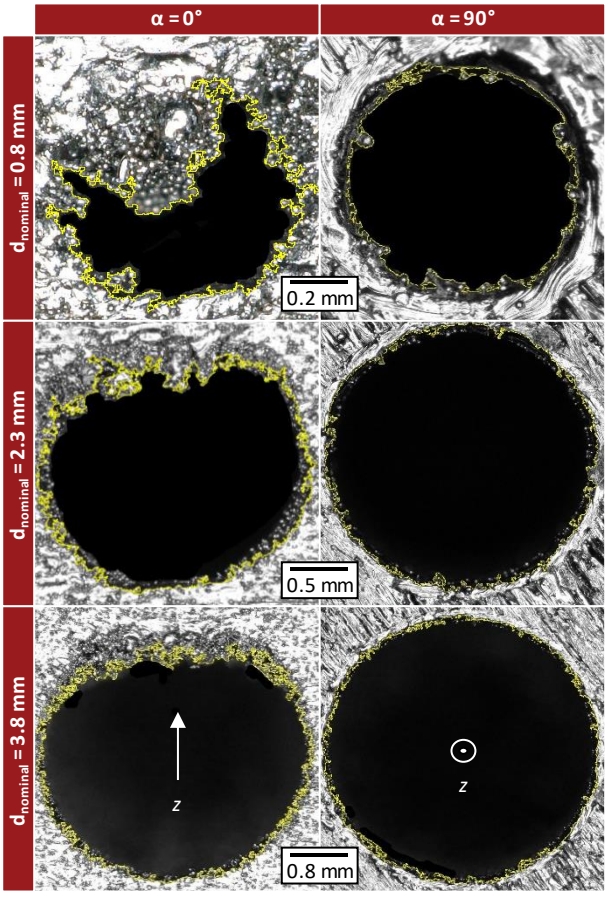

Figure 6. LOM images and analysis of three different nominal channel diameters $d_{nominal}$ = 0.8, 2.3 and 3.8 mm for α = 0° and 90° on the B-artefact

Figure 7 shows the cross-sectional reduction of the actual measured area when compared to the area of a circle with $d_{nominal}$. The observed reductions for α = 0° are systematically higher than for α = 90°. Both graphs are following a similar curvature. The reduction of cross-sectional area for α = 0° is decreasing steeply from 58 % at $d_{nominal}$ = 0.5 mm until approximately $d_{nominal}$ = 1.7 mm. Thereafter, it reaches a plateau at approximately 16 % on average between $d_{nominal}$ = 1.7 mm and 4.1 mm. The curve for α = 90° is decreasing from 16 % at $d_{nominal}$ = 0.5 mm until $d_{nominal}$ = 1.4 mm. Thereafter it reaches a plateau at approx. 4 % on average between $d_{nominal}$ = 1.4 mm and 4.1 mm.

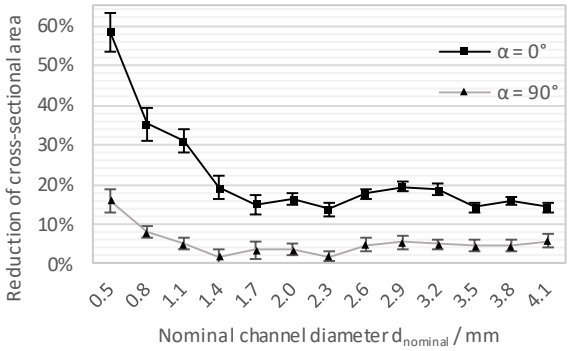

Figure 7. Influence of $d_{nominal}$ on cross-sectional area reduction α = 0° and 90°, measurements are based on B-artefact and LOM image analysis

It can be seen that the influence of the channel direction α is decreasing with increasing channel diameters. The non-linear scalability has been visualized in figure 8 by plotting the ratio between the actual cross-sectional area for α = 0° and 90°.

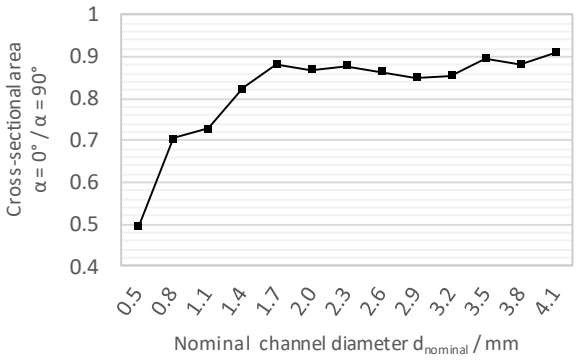

Figure 8. Non-linear scalability of the build direction effect regarding actual cross-sectional area

5. Discussion of results and translation to prediction model

First, the presented results are discussed with respect to the different applied methods. Finally, the results from the A- and B-artefact are validated and translated into a lookup table with correction factors.

The unintended sintering of metal powder particles onto the channel walls causes form deviations and subsequently decreases the cross-sectional area. The channel direction relative to the build direction has a direct impact on the magnitude of this effect with α = 0° being most pronounced. These effects on the cross-sectional area decline with larger nominal channel diameters indicating a limited amount of powder particles with a constant size being sintered onto the channel wall each time. According to the formula for the area of a circle, the effect on the reduction in cross-sectional area of the channel should decline in a quadratic manner. However, the

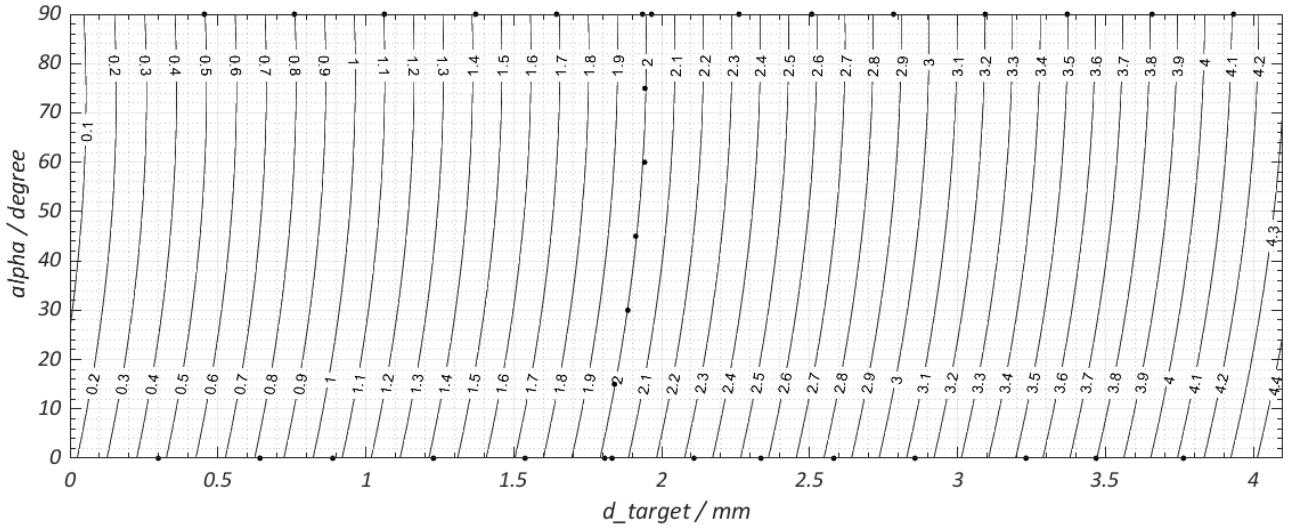

Figure 9. Corrected design parameter d* dependent on intended cross-sectional area with d_{target} and channel direction α

measurements in section 4 rather suggest a constant reduction for channel diameters being larger than $d_{nominal}$ = 1.7 mm. The limited resolution of the measuring method can serve as an explanation in this instance. Larger channel diameters require the use of lower magnifications that fail to capture single sintered powder particles along the channel perimeter. Additionally, the field of depth increases at lower magnifications leading to an overestimation of sintered particles along the channel perimeter.

For $d_{nominal}$ = 2 mm the A- and B-artefact share an equal feature for validation purposes. Table 2 provides a comparison between both applied methods in this work. The results from the CT-method are based on 500 consecutive cross-sectional measurements along the channel direction. In general, these measurements resulted in a lower standard deviation when compared to the LOM-method using three measurements in one plane instead.

Table 2. Comparison of reduced actual cross-sectional area between CT- and LOM-method based on the same feature with $d_{nominal}$ = 2.0 mm

α	A-artefact (CT)	B-artefact (LOM)
0°	- 16.05 ± 1.22 %	- 16.31 ± 1.56 %
90°	- 3.38 ± 0.36 %	- 3.63 ± 1.39 %

Finally, based on the measurements of both artefacts, a second-degree polynomial function

$$(2) \quad d^*\left(d_{target}, \alpha\right) = 0.1758 + 0.9902\, d_{target} - 0.00351\, \alpha + 0.0155\, {d_{target}}^2 - 0.00023\, d_{target}\, \alpha + 0.00002\, \alpha^2$$

is fitted to the observed data with an R^2-value of 99.94 %. The function determines the corrected design parameter d^* based on the chosen channel direction α and the intended cross-sectional area expressed as the diameter d_{target}.

In figure 9, the prediction model is plotted to serve as a lookup table to identify the corrected channel diameter d^* which can be read from the contour lines. The dots represent the experimental design and data used in this work.

5. Conclusions and future work

In this work, two test artefacts and two different methods to extract the cross-sectional area of additively manufactured channels have been introduced and applied. By means of the first artefact (A), it was shown that the cross-sectional area scales linearly from being the smallest perpendicular to the build direction (α = 0°) and the largest parallel to the build direction (α = 90°). On the basis of the second artefact (B), the scalability of the build direction effect was investigated dependent on the nominal channel diameter. It was shown that the influence of build direction on the cross-sectional area is declining with larger channel diameters in a non-linear manner.

Finally, based on both artefacts and methods, a prediction model was derived and presented in the form of a contour plot. Under the constraint of keeping the process-parameters constant, the contour plot serves as a lookup table to upscale the diameter accordingly to compensate for the reductions of cross-sectional area in channels in future build jobs.

Future work includes further validation of the derived prediction models. While the A-artefacts were designed for detailed CT-scanning analysis, the B-artefact allows a more rapid and resource efficient analysis via LOM in terms of evaluating the cross-sectional area of AM channels. Therefore, the methodology can also serve as a standard for benchmarking and process optimization regarding additively manufactured channels in the future.

Acknowledgments

The 3D Imaging Center at The Technical University of Denmark is acknowledged for their assistance in X-ray CT-scanning.

References

[1] Dimla D E, Camilotto M and Miani F *J. Mat. Process. Tech.* **164-165** 1294 - 1300
[2] GE Reports 2015 *http:// www.gereports.com /post / 1164 0 2870270 /the-faa-cleared-the-first-3d-printed-part-to-fly*
[3] Schmelzle J, Kline E V, Dickman C J, Reutzel E W, Jones G and Simpson T W 2015 *Metal Add. Manuf.* **137** 111404
[4] Achenbach E 1971 *J. fluid mech.* **46** N2 321-335
[5] Snyder J C, Stimpson C K, Thole K A and Mongillo D J 2015 *J. Mech. Design* **137** 111411
[6] Strano G, Hao L, Everson R M and Evans K E 2013 *J. Mat. Process. Tech.* **231** 589-597
[7] Snyder J C, Stimpson C K, Thole K A and Mongillo D J 2016 *J. Turbomach.* **138** 5 051006
[8] Klingaa C G, Bjerre M K, Baier S, De Chiffre L, Mohanty S and Hattel J H 2019 *e-J. Nondestruct Test.*
[9] Schneider C A, Rasband W S and Eliceiri K W 2012 *Nature Meth.* **9**, 671-675